International Journal of Robotics and Automation, Vol. 40, No. 10, 2025
An Open Access Paper

MODEL OF A HUMAN WRIST FOR ESTIMATING FORCE FEEDBACK IN HUMAN–ROBOT INTERACTIONS

Zachary Ochitwa,* Reza Fotouhi,* and Haron Obaid**

Abstract

This research is part of the musculoskeletal tele-robotic imaging machine (MSK-TIM) project. The MSK-TIM is a device that facilitates remote ultrasound diagnosis through remote control of an ultrasound probe. The work reported here is to facilitate human–robot interaction in remote ultrasound imaging. To reduce the overall examination time, areas of improvement include improving the intuitiveness of control via haptic feedback, mitigating delay, and improving training. This work investigates developing a virtual model which can be used for these purposes. Developing a model to understand the biomechanics of the patient's wrist is important in several fields including medicine and robotics. Up to now, most models have been developed to accurately represent the complex internal structure of the wrist. However, there are several applications, such as generating a force for haptic feedback, informing a predictive controller to mitigate delay, or providing a simulated training environment, which requires a rapid solution. This study reports on investigation on how we developed a finite element wrist model to test the feasibility of a force-feedback control for a remote ultrasound system. The geometry and material parameters of the human wrist were obtained in vivo. The finite element model was then incrementally modified to improve the computational time while measuring the corresponding error. As a result, the computation time was reduced by 95%. As a result of this study, it has been shown that soft tissues can be generalised as a phenomenological material to decrease model complexity. The average first-order Ogden parameters for soft tissue in the wrist were derived to be (μ, $\alpha 1$) = (4.59 kPa, 10.69). Finally, the geometry of anatomy can be simplified, without a major reduction in accuracy, to greatly reduce the computation time.

Key Words

Human–robot interactions, finite element, wrist model, biomechanics, haptics

* Department of Mechanical Engineering, University of Saskatchewan, Saskatoon, Canada; e-mail: zachary.ochitwa@usask.ca; reza.fotouhi@usask.ca
** Department of Medical Imaging, University of Saskatchewan, Saskatoon, Canada; e-mail: haron.obaid@usask.ca
Corresponding author: Reza Fotouhi

Recommended by Chris W. J. Zhang
(DOI: 10.2316/J.2025.206-1221)

1. Introduction

The human wrist is a complex joint, consisting of many different tissues and capable of many various configurations. However, it is also indispensable in everyday life. The wrist is used to grasp, pick up, and move objects; it is through the wrist that most people interact with the world around them. Unfortunately, the wrist is also subject to many different injuries or diseases. Therefore, it is important to model the wrist to understand its mechanisms, prevent injury, and assist in future treatments.

There are several different types of wrist models, each with their own objectives. One area of recent interest is developing an anatomical wrist model to understand its complex, underlying mechanisms. This allows for the study of the wrist without live subjects or cadavers. One application of such a model is to study the mechanism of injury and inform rehabilitation. For example, the model in [1] studied the load distribution in the carpal bones in different wrist positions to help explain fractures. Similarly, the model in [2] looked at the strength of the scaphoid bone at different stages of healing from a fracture to inform rehabilitation decisions. Wrist models have been used to investigate diseases such as the ones developed in [3] and [4] to study carpal tunnel syndrome. Finally, physics-based wrist models have been used to investigate medical procedures. For example, [5] simulated a wrist with a four-corner arthrodesis implant and found that one insertion orientation resulted in much lower stress. Physics-based models can be used to predict novel conditions through an understanding of the underlying mechanics as opposed to data-based or statistical models [6]. The finite element method is typically used in these types of models due to its flexibility, especially with complex geometry [7]. Factors, such as types of loads, orientation and proportion of geometry, or utilised material models can be adjusted within a finite element model.

In summary, anatomical models are a useful tool with several different applications. This is especially true for the wrist, a crucial joint that is subject to many pathologies. The previously mentioned wrist models were developed with the objective of increasing accuracy or

resolution. However, this is typically in exchange for a higher computational resource cost or a longer time to calculate. The models in [6], [8], [9] used 122,000, 3,52,000, and 1,640,000 elements, respectively, with the latter reporting 496 central processing unit (CPU) hours to solve. This is necessary to understand the fine details, such as how a load is transferred throughout the many constituent components in the joint. However, some use cases do not require a detailed understanding of the interior structure. Instead, a simplified model may be sufficient or even required to meet time constraints. One method to create a more computationally efficient model is to design a phenomenological model. Instead of modelling the geometry and contact between layers of skin, muscle, and other soft tissue independently, they could be modelled as a generalised soft tissue in the wrist [10]. The bony structure could also be simplified depending on the need. This can greatly speed up the computation time in exchange for losing detail at the microscopic level.

This research was conceived as part of the musculoskeletal tele-robotic imaging machine (MSK-TIM) project at the University of Saskatchewan Robotics Lab. The MSK-TIM is a device that facilitates remote ultrasound diagnosis through remote control of an ultrasound probe [11]. Through this technology, locations with a shortage of trained specialists, such as remote or rural locations, can still receive required care. A model of human anatomy was noted to have three main applications for this project: haptic feedback, manipulator control scheme, and a virtual sensor. In a conventional ultrasound, tactile feedback is used to feel around the patient's anatomy and navigate the ultrasound probe. However, in robotic ultrasound, this tactile information is lost as the radiologist no longer holds the probe. Haptic feedback re-introduces tactile information partially to the operator through a haptic interface. The force input to the haptic device can be generated by a virtual model. Haptic feedback in remote systems result in more intuitive control, access to palpation, and lower forces applied to the patient [12], [13]. A mathematical model can also improve the control of the manipulator. For example, such a model can be used to predict future states of the system. A predictive controller can be used to mitigate the effects of latency or provide delay-compensated force-feedback [14]. Finally, the model can be used as a virtual sensor for other applications. For example, if the estimated load exceeds a given threshold, it could prevent further motion which could harm the patient. Safety within human-robot interactions is of the utmost importance and special consideration should be given when there is contact [42]. Alternatively, this virtual sensor can be used in environments such as training simulations like proposed in [43]. A physical load cell is a well-established technology; however, it cannot be used in all circumstances. A load cell cannot be mounted in some locations, such as at the end effector of an ultrasound probe; also integrating load cells to measure multiple degrees of freedom (DOF) can drastically increase complexity. Manipulators from third parties may also be difficult to integrate a load cell to them. Load cells may also see errors arising from other factors, including temperature change, noise/vibration, hysteresis, or incorrect mounting. In contrast, a virtual sensor or model requires less hardware, can predict future or novel states, and can provide a larger breadth of information, if needed. For example, a mechanical model can predict the stress distribution in areas of contact, instead of a single number for force or pressure. The finite element method was chosen since it can potentially account for differences between patients or changes in wrist orientation. Therefore, this research will test the feasibility of using a finite element mode of the wrist to predict the contact force.

In addition to the applications relevant to the MSK-TIM project, there are several other uses for modelling the interaction of the wrist with its external environment. An example of this is virtual training environments for medical techniques. With this simulation, a medical practitioner can practice skills and procedures without special equipment or materials [15], [16]. However, to operate smoothly, the computations should be solved quickly. One final application comes in the form of physics-based animation which excels at flexibility and simulating contact between bodies compared to data-based animations [6], [17]. This is especially valuable if the same modelling techniques can be applied to other anatomy or composite structures. Therefore, it is valuable to develop a quick model for simulating contact forces as opposed to a slower, comprehensive model.

As part of the MSK-TIM project, this study will specifically study how the model can predict the contact forces for robotic ultrasound. This study will include: (1) measuring the force-displacement curve of a human arm-probe interaction experimentally, (2) creating a representative finite element model of the arm, and (3) simplifying the representative model with the goal of minimising the computational time.

2. Materials and Methods

2.1 MSK-TIM Device

The experimental force-displacement data was obtained using a robotic manipulator—the MSK-TIM. This device was developed by the Robotics Lab at the University of Saskatchewan to research and develop robotic tele-ultrasound technology [18]. The manipulator that holds the ultrasound probe is a 4-DOF robot manipulator with three prismatic joints and one revolute joint, as seen in Fig. 1(a). A 1-DOF compression load cell was installed to measure the force applied to the probe in the vertical axis. This can be seen in Fig. 1(b). The load cell is designed to measure up to 15 lb (67 N) based on expected loads during ultrasound applications [19], [20]. The mean round-trip delay was measured to be 26 ms [11].

In this study, the MSK-TIM was used to measure the non-linear stiffness of a human wrist. The applied force was measured using the integrated load cell while the corresponding displacement was measured using a dial gauge, recorded by a video camera. The probe was lowered onto the subject's arm at a rate of 0.004 in/s (0.1 mm/s) until the measured applied load exceeded 12 pounds (53

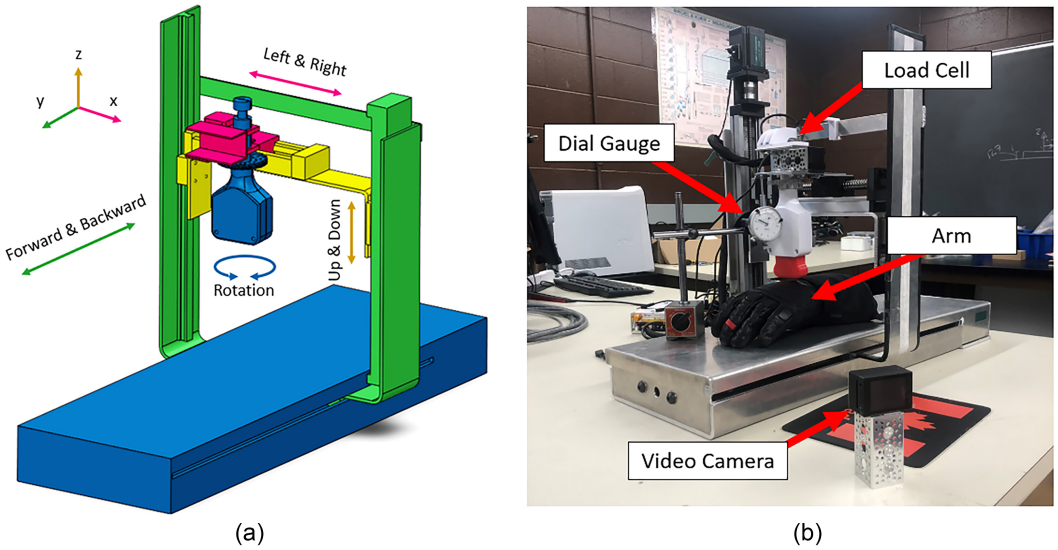

Figure 1. MSK-TIM demonstration of (a) available degrees of freedom, and (b) the experimental set-up.

N). This procedure was chosen to stay within a quasi-static loading scenario and was repeated at least 10 times for each location. The load cell recorded force data at a frequency of 30 Hz. The video camera recording displacement of the dial gauge was operating at a frequency of 60 Hz. Three locations were considered for this experiment: the distal head of the ulna, 1 inch (2.5 cm) distal, and 1 inch (2.5 cm) proximal of the ulna head. These locations, going from the most distal to proximal, will be identified as locations one, two, and three, respectively. Throughout the entire experiment, the width of the probe was orientated in the transverse direction across the wrist.

2.2 Finite Element Model Construction

After obtaining the experimental stiffness data, a finite element model was developed to replicate the human arm-probe interaction (a human–robot interaction function). The purpose of this model is to predict the contact force given the probe displacement into the arm. The goal is to develop a model that returns the same results as the experimental test with a small computation time.

2.2.1 Geometry

The model of the arm consists of two components: the soft tissue, and the bony structure within.

The exterior of the soft tissue was generated by replicating the subject's arm using photogrammetry, a technique that creates a three-dimensional (3D) model from multiple photographs of different perspectives. A total of 287 photographs were uploaded into a photogrammetry program (Meshroom) to create a mesh of the arm with 600,000 triangles, as shown in Fig. 2. The mesh was simplified and converted into a solid body defined by 17,000 elements. The body was cut near the fingers and elbow since they were unnecessary for the analysis and increased the size of the model. The bony structure within the arm was modelled as a single solid structure which was approximated using MRI photos from the literature [21]. It was hypothesised that only the shape of the bone under the probe had a substantial effect on stiffness; and that the bone away from the probe has a negligible impact. Therefore, a constant cross-section was extruded throughout the arm. The bone was placed in the arm and a Boolean operation was used to remove the soft tissue where bony tissue was present. Three models were generated to represent the three test locations. The ultrasound probe geometry was generated based on measurements of the Phillips Lumify L12-4 transducer.

2.2.2 Material Properties

As mentioned earlier, soft biological tissue expresses non-linear elastic behaviour. Therefore, an energy-based method called hyper-elasticity is typically used. The governing equation for hyper-elasticity is:

$$S = \frac{\partial W}{\partial A}(A), \tag{1}$$

where $\boldsymbol{S}$ is the nominal stress tensor, also known first Piola–Kirchhoff stress tensor, W is the strain energy per volume, and $\boldsymbol{A}$ is the deformation gradient tensor [22]. Within hyper-elastic theory, there are several different models which define the function W. In this study, the Ogden model will be used since it has been shown to have relatively good accuracy and a reasonable amount of reference material in the literature [23]–[25]. The first-order Ogden model is given by:

$$W\left(\lambda_1, \lambda_2, \lambda_3\right) = \frac{2\mu}{\alpha_1^2}\left(\lambda_1^{\alpha_1} + \lambda_2^{\alpha_1} + \lambda_3^{\alpha_1} - 3\right), \tag{2}$$

where λ_i are the principal stretches, μ is the initial shear modulus, and α_1 is a phenomenological material property that defined the Ogden model. Note that the two material parameters μ and α_1 dictate the non-linear stiffness of a material and are comparable to Young's modulus for a linear elastic material. The analytical model used in the

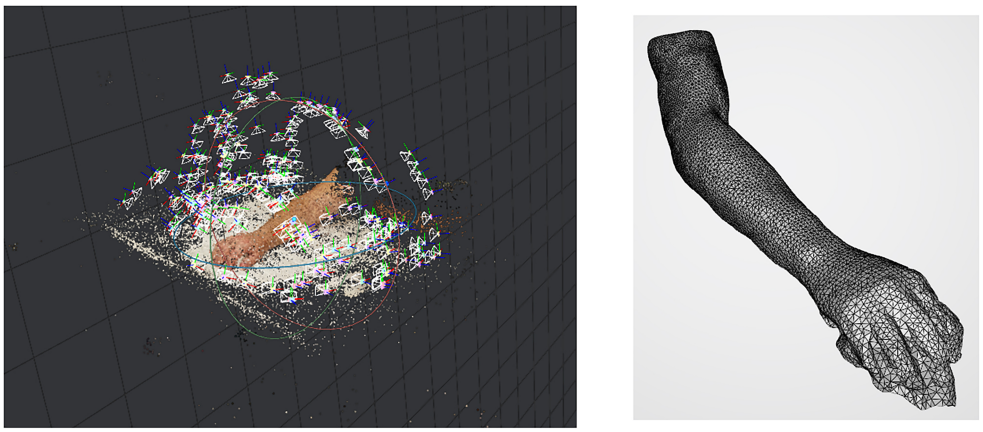

(a) (b)

Figure 2. Human arm model photogrammetry: (a) construction of geometry including the perspectives taken and (b) the resultant geometry generated.

convergence analysis assumed an incompressible material, due to the tissue water content, which experiences uni-axial compression [26]. The component of normal stress on the skin's surface from a compressive load was derived to be:

$$\sigma_{11} = \frac{2\mu}{a_1}\left(\lambda_1^{a_1} - \lambda_1^{-\frac{\alpha_1}{2}}\right), \tag{3}$$

where σ is the Cauchy stress tensor.

Several papers have reported the first-order Ogden parameters for human tissue, varying by location or tissue type. It was hypothesised that the material parameters derived from the wrist should be comparable for similar tissues. Therefore, the material parameters found in the wrist will be compared to the literature. The material parameters of similar tissue can be found in Table 1.

Studies [27]–[29] used the same approach as this study, measuring the load and corresponding displacement during a compressive load. References [30] and [31] conducted a biaxial tension test and a tension test, respectively while using digital image correlation (DIC) to measure the corresponding displacement. All these studies then used inverse finite element analysis (FEA) to obtain the material parameters. To the co-authors' knowledge, no study has obtained the first-order Ogden material parameters for the wrist.

In contrast to the soft tissue, the bone was modelled as a linear elastic material. However, bone is anisotropic and exhibits different stiffnesses in longitudinal and transverse loading. The stiffness of cortical bone in transverse loading has been reported from 5.1–24.6 GPa [32]–[34]. A Young's modulus of 15 GPa and a Poisson ratio of 0.3 were chosen based on ranges commonly used for cortical bone in wrist modelling [7]. It was hypothesised and later confirmed, that the bone deforms negligibly compared with the soft tissue. Therefore, the material properties of the bone do not have to be as precise as the soft tissue.

2.2.3 Meshing and Boundary Conditions

The meshing and FEA was done using the static model in ANSYS 2022 R1 (FEA-A). The computer used in

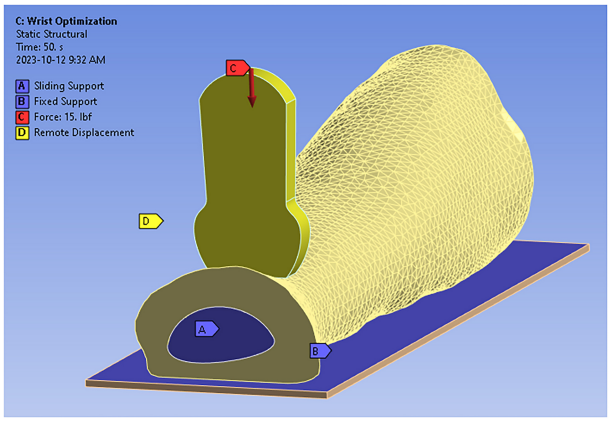

Figure 3. Boundary conditions of the finite element model including the load, fixed base support, sliding support at ends, and remote displacement on the probe.

the simulation included an Intel i7-8700 CPU a GeForce GTX 1660 graphics processing unit (GPU), and 32 GB of DDR4 random access memory (RAM) at 2666 MHz. The calculations were distributed over four cores.

In Fig. 1(a) and in FEA, the x, y, and z-axis correspond to the distal-proximal axis (or down the length of the arm), transverse (or across the arm), and in the vertical direction, respectively. The vertical load was applied to the arm through the ultrasound probe at a range of 0 to 15 lb-f (67 N), at increments of 0.3 lb-f (1.3 N). The motion of the probe was limited to the vertical axis. Underneath the arm was a solid body which was the ground for the experiment. A displacement boundary condition was set on the y-z planes corresponding to the cuts made at the fingers and elbow. At these boundary conditions, the bone was prevented from displacing in the x-axis. These loads and boundary conditions can be seen in Fig. 3.

Three contact regions were defined in the model, shown in Fig. 4. These are the contacts between the soft tissue and the ground, bone, and probe, respectively. The contact region with the ground was created to fix the model

Table 1
First-Order Ogden Parameters of Human Soft Tissue from the Literature

ID	μ (kPa)	α_1	Tissue	Derivation Technique
Skin 1 [27]	5.07	9.14	Human muscle, 90° to fiber direction	Compression load
Skin 2a [28]	2.60	35.9	Anterior human lower forearm	Compression load
Skin 2b [28]	39.8	33.5	Anterior human upper forearm	
Skin 2c [28]	9.60	36.0	Posterior human arm	
Skin 3 [29]	4.10	23.0	Human finger	Compression load
Skin 4 [30]	23.5	-14.5	Human skin	Equi-biaxial tension load
Skin 5 [31]	0.13	26.0	Human arm	Tension load

and dynamically adjust the contact area with the ground depending on the load. The second bonded contact was required for the bone to provide stiffness to the model. The third bonded contact with the probe allowed the load to be transferred to the arm model in a way that simulates the experiment.

The mesh size of the bone and soft tissue was determined based on a convergence analysis comparing the simulation to analytical theory. Both methods applied a 15 lb (67 N) uniaxial compressive load on a rectangular body of approximately the same dimensions as the original arm model. The resulting probe-end displacement was measured. A mesh size of 0.15 inches (3.88 mm) was chosen, which corresponded to an absolute error of under 1%, and can be seen in Fig. 5.

2.3 Deriving Material Parameters

While the first-order Ogden parameters of human soft tissue have been reported in the literature it would be good to determine the value of the parameters which can be extracted from our experimental data. The benefit of this is two-fold.

1. The literature does not have the material parameters for soft tissue at the wrist. This would add to the body of literature and help identify changes based on location.
2. Deriving the parameters can be used to compare against the literature to verify the experimental data and finite element model.

The goal of the material optimisation is to find the material parameters (μ, α_1) which most closely resembles the experimental data. Error will be measured using root mean square error (RMSE). Therefore, the objective function is:

$$\text{MIN } E(\mu, \alpha_1) = \sqrt{\frac{\sum_{i=1}^{n} \left(P_e(x_i) - P_s(x_i, \mu, \alpha_1)\right)^2}{n}}, \quad (4)$$

where $E(\mu, \alpha_1)$ is the RSME, n is the number of experimental data points taken, $P_e(x_i)$ refers to the experimentally measured force value corresponding to the ith measured displacement x_i, $P_s(x_i, \mu, \alpha_1)$ refers to the simulated finite element contact force at the same displacement as $P_e(x_i)$. Variable μ is the initial shear modulus and α_1 is a material parameter.

In summary, this function compares the experimentally measured and simulated forces at the same displacement for the entire range of experimentally measured displacements. This curve-fitting procedure is constrained by $|\alpha_1| > 1$ since strain-hardening is expected for a compression load [35].

The Nelder–Mead optimisation method was used to find values of μ, α_1 which results in a simulated force-displacement curve that best fits the experimental data for each three locations. A detailed description of this optimisation procedure can be found in Appendix 1. Note that the accuracy of the curve-fitting is dependent on the accuracy of the experimental data. Three initial points were selected from Table 1 to provide the biggest range. These initial points are (μ $[kPa], \alpha_1$) = (5.07, 9.14), (39.8, 33.5), and (0.13, 26.0). For each location, the curve-fitting algorithm was repeated until two conditions were both met: First, the standard deviation of the RMSE across the 3-point simplex must be less than 1% of the mean. Second, the standard deviation of the final parameters across the 3-point simplex must be less than 10% of the mean. The procedure used to derive the material parameters from experimental data can be seen in Fig. 6.

2.4 Finite Element Model Simplification

As mentioned earlier, the goal is to make a computationally efficient finite element model. While the model started with a 3D scan of a human arm, it was hypothesised that the model could be simplified to decrease the computation time. With a quicker solution, the system relying on the model data can react faster to more recent information. For example, in haptic feedback, a large delay would mean that the operator is reacting to outdated information which makes it difficult and time-consuming to palpate. On the other hand, a virtual sensor with frequent updates would quickly determine if the applied load exceeded a safety threshold. This fast response is essential for real-time applications. Note that the computation time is not only dependent on the complexity of the model but also the capability of the host computer.

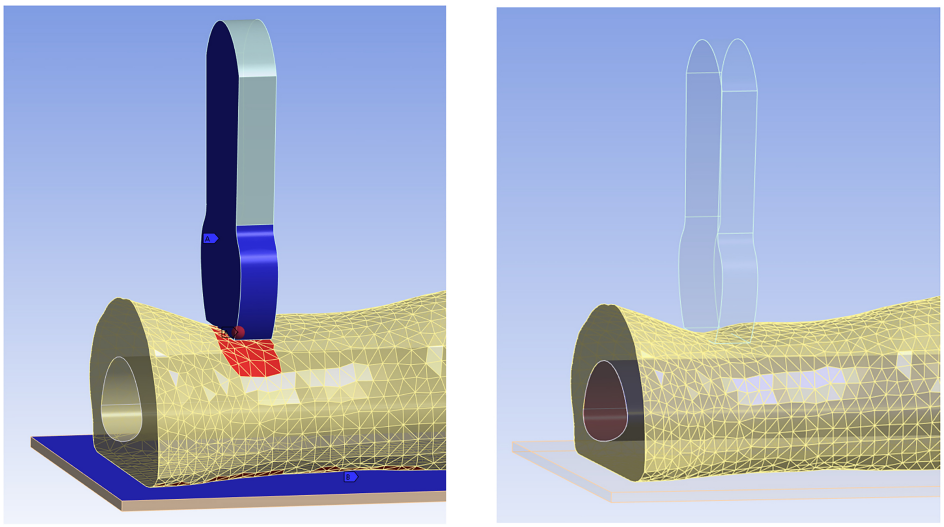

Figure 4. Contact Regions of the (a) probe-soft tissue and base-soft tissue interactions and (b) bone-soft tissue interaction.

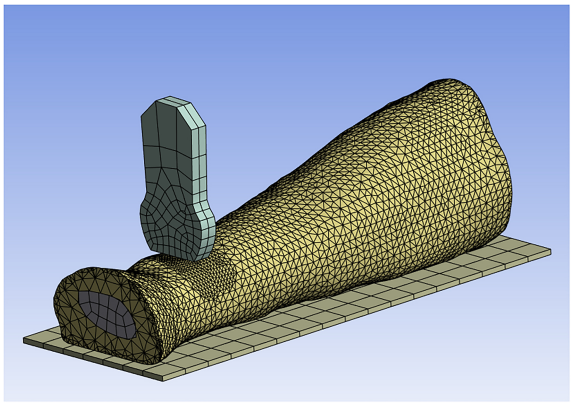

Figure 5. Mesh of the finite element model for location 3.

While simplifying the model decreases the computation time, it often decreases the accuracy of the model. However, knowledge of the application can help make informed decisions that limit the impact on the accuracy of the model. For example, if a model is symmetrical, at least half the geometry can be removed with negligible impact on accuracy. In the case of modelling complex geometry like the human arm, several simplifications can be made but the effects are not well understood.

This section will investigate several incremental modifications made to the original model created in Section 2.3. Both the difference in computation time and deviation from the original stiffness curve will be measured. As a result, this experimental approach will not only measure the effectiveness of simplifying the model but also help to evaluate if such a change is appropriate. This can help to inform future designers on how to build an appropriate model for their cases.

In this part of the study, four primary models were considered. These were given the names: 1. cylindrical model, 2. multi-slab model, 3. top-reduced model, and 4. halved model. The purpose of this experiment is to investigate how simplifications may change the result of the original model. Therefore, the reported error will be the RMSE between the original force-displacement curve and the modified force-displacement curve. As with the original model, the applied load is set as a boundary condition while the displacement will be the output of the simulation.

The cylindrical model, seen in Fig. 7(a), is visually mostly like the original model. This model's main identifying feature is that both the soft tissue and bone have a constant cross-section throughout the model. This is obtained by extruding the cross-section at the center of the probe through the entire length of the model. All three locations have a different model. The main assumption made in this model is that the local geometry underneath the probe is the dominant contributor to stiffness, in contrast to the changes in geometry down the length of the arm, which have a negligible impact on stiffness. This model could potentially be reduced to a two-dimensional model like in [36].

The second simplified model is the multi-slab model which consists of three laminated slabs as seen in Fig. 7(b). The top and bottom slabs are made of soft tissue while the middle slab is made of bone. This model was created by eliminating the soft tissue to the left and right extremities of the bone. The three components are each replaced with rectangular slabs of a set thickness. The thickness of the middle slab is set as the average thickness of the bone while the thickness of the top and bottom slab combined is set as the average thickness of the total soft tissue. For example, in location 1, the average bone thickness was 0.627 in (15.9 mm) and the average total soft tissue thickness was 0.659 in (16.7 mm). The relative position of the bone within the soft tissue was a variable and was chosen to minimise RMSE with the experimental data. Future research could involve investigating whether the "average" thickness is the best choice.

When modifying the cylindrical model to the multi-slab model, the "ground" body is removed, and a fixed boundary condition is set on the bottom surface. This model assumes that the skin to the left and right of the

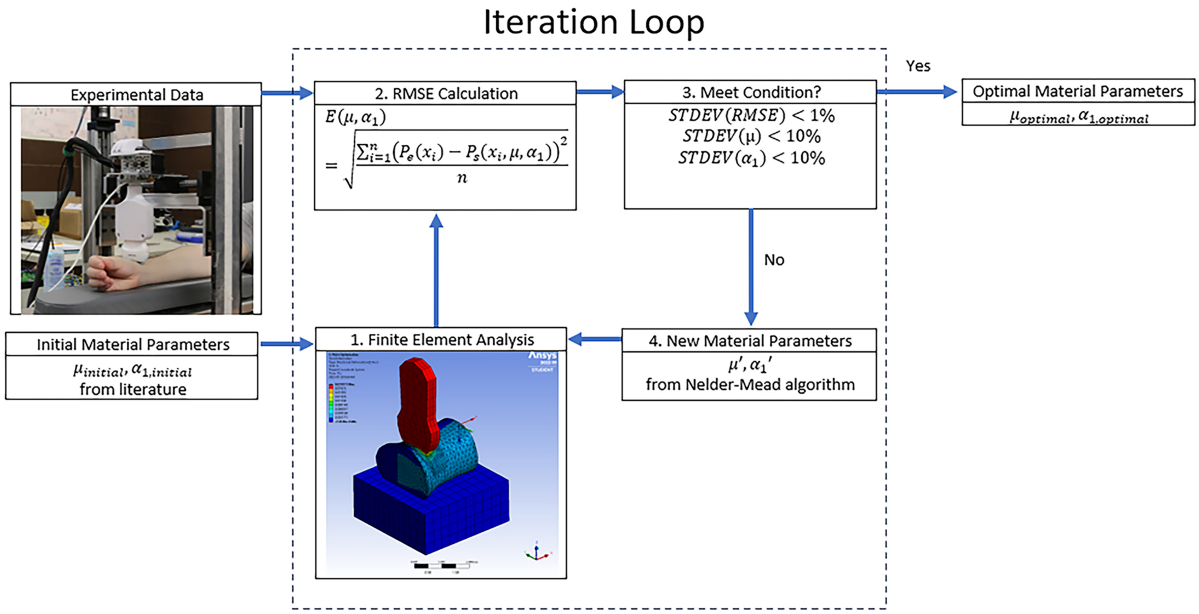

Figure 6. Inverse finite element analysis procedure to obtain material parameters.

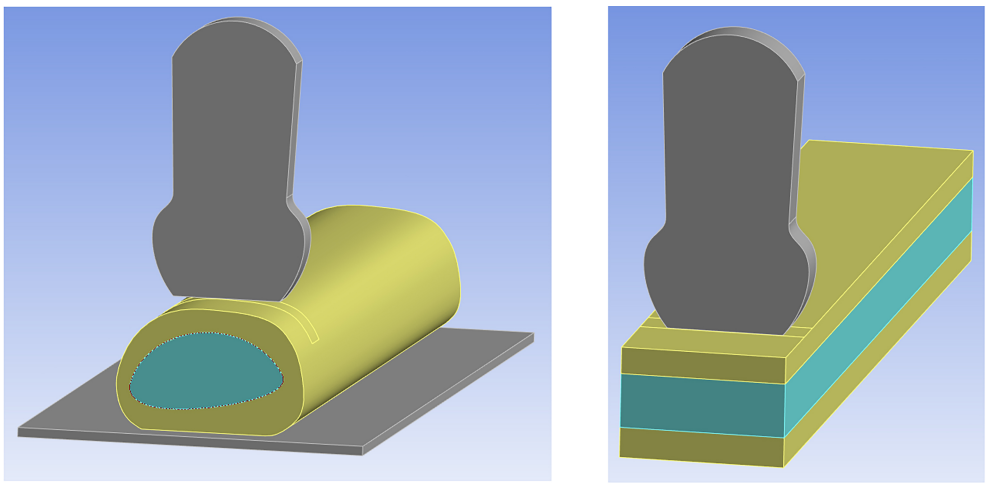

Figure 7. Simplified FE models 1 and 2: (a) cylindrical model and (b) multi-slab model.

bone extremity provides negligible stiffness. In addition, it assumes that the asymmetrical geometry of the bone-soft tissue interface can be approximated as a flat surface.

However, there are two main differences: the bone is rigid, and the length of the top slab is reduced, as shown in Fig. 8(a). This model assumes that only the skin near the probe face provides structure to the model. Therefore, the top-slab elements further away from the probe face can be removed. This model also makes use of the fact the bone contributes negligibly to the wrist's deformation. The multi-slab finite element model predicts that the bone contributes under 0.01% of the total deformation at 15 lb (66.7 N), thus it can be assumed to be rigid.

The fourth and final simplified model, the halved model, is a continuation of the previous model. However, half of the model was removed, and both the bone slab and bottom slab were shortened, as seen in Fig. 8(b). This model makes use of symmetry to reduce the total number of elements. Half of the entire model in the transverse direction was removed and the loading scheme was reduced by a factor of 2. An appropriate (sliding) boundary condition is applied to the cut surface. Additionally, since the load is applied to one end of the arm, it is assumed that the tissue on the other side contributes less. Therefore, elements from both the bone and bottom slab can be removed on the opposite side of the probe without affecting the results, noticeably.

3. Results

3.1 Experimental Results

The mechanical response of the human arm under load was investigated both experimentally and numerically. The force-displacement response obtained from physical experiments can be seen in Fig. 9. The measured data for

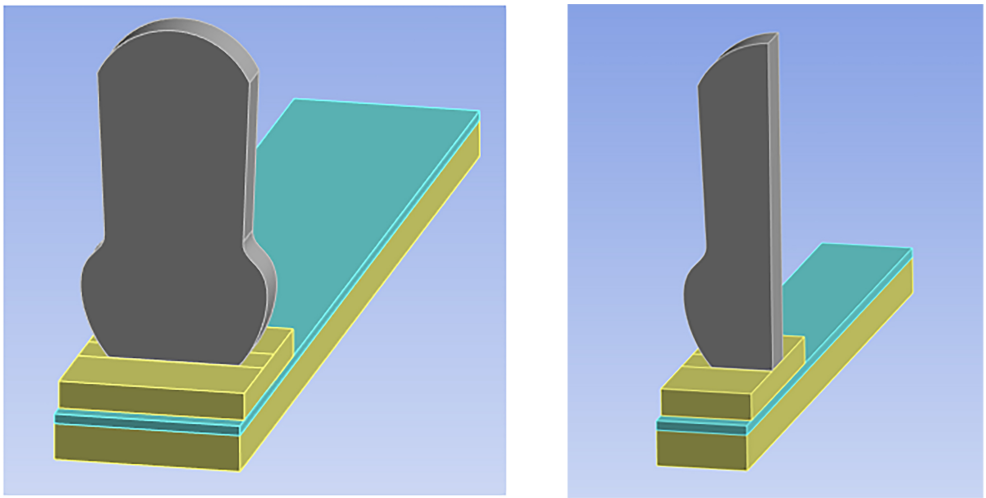

Figure 8. Simplified FE models 3 and 4: (a) top-reduced model and (b) halved model.

location 1 is indicated by the blue curve, location 2 is orange, and location 3 is yellow.

As can be seen, locations 1 and 2 have relatively similar stiffness profiles while location 3 is generally less stiff. This was expected as location 3 has more volume of soft tissue. Accounting for the difference in the probe contact area, the range and shape of the curve are similar to other experiments on the arm in the literature. This is especially true for measurements at location 3 in this study and the lower anterior forearm reported by [28] which are both measurements of the lower forearm. Variation in the measurements can be attributed to slight changes in the position or orientation of the arm relative to the probe as well as noise from the amplified load cell signal.

3.2 Finite Element Results

Asa result of the convergence analysis, a mesh size of 0.15 inches (3.8 mm) was chosen. At this size, the finite element model had an absolute percent error under 1% compared to analytical theory. The measure of error and computation time with the reciprocal of mesh size can be found in Fig. 10. The mesh was additionally refined at the contact area between the probe and soft tissue to accurately capture local phenomena, as can be seen in Fig. 5.

The finite element model was used to predict the non-linear stiffness characteristics of the human wrist. This was first done with material parameters from the literature to roughly validate the model. For each material parameter, a forward FEA was conducted to calculate the resultant force-displacement curve. An example of the deformed model in the FEM program can be seen in Fig. 11(a). Fig. 11(b) shows the force-displacement curve generated within the finite element program. The applied force is an input while displacement is the measured output of the model. Specifically, the force on the y-axis is the load applied to the top of the ultrasound probe as shown in Fig. 3. The displacement on the x-axis is the average displacement, also across the top of the probe, which is a result of the applied force. As expected, the stiffness increases under a compressive load which suggests strain-stiffening [35].

This procedure was repeated for all material parameters in Table 1 which was then compared to the experimental data. An example comparison for location 1 can be seen in Fig. 12. This Figure also shows the results of the convergence analysis. As can be seen, the experimental results fall within the range of what was predicted using the material parameters from the literature. Similar results occurred for location 2 and location 3. Note that the material parameters vary for multiple reasons: the type of tissue being measured, the location of the tissue, the technique to measure stiffness, and the finite element model.

Following the forward finite element model to verify the model, a finite element model correction (or inverse FEA) was conducted to derive material parameters from the experimental data. Locations 1, 2, and 3 took 21, 29, and 35 iterations, respectively to meet the end condition. As the material parameters were converging on a solution, the resulting force-displacement curve aligned with the experimental data as shown in Fig. 13(a)–13(c). The Nelder-Mead algorithm uses three test points for 2-parameter optimisation. Fig. 13(d) shows how the average RMSE decreases and converges across iterations on a semi-log graph. Uncertainty in the experimental data contributed to "error" in curve fitting. With more precise equipment, the RMSE most likely will decrease.

As a result of optimising the static finite element model of the arm-probe interaction, the first-order Ogden material parameters were obtained; which are the converged values shown in Table 2.

These results generally lie within the range given by the parameters in Table 1. The α_1 parameter is relatively similar between locations. However, the shear modulus for location 1 is larger than for locations 2 and 3 which suggests that a stiffer tissue is present. The average first-order Ogden material parameters across all three locations are $(\mu, \alpha_1) = (4.59 \text{ kPa}, 10.69)$.

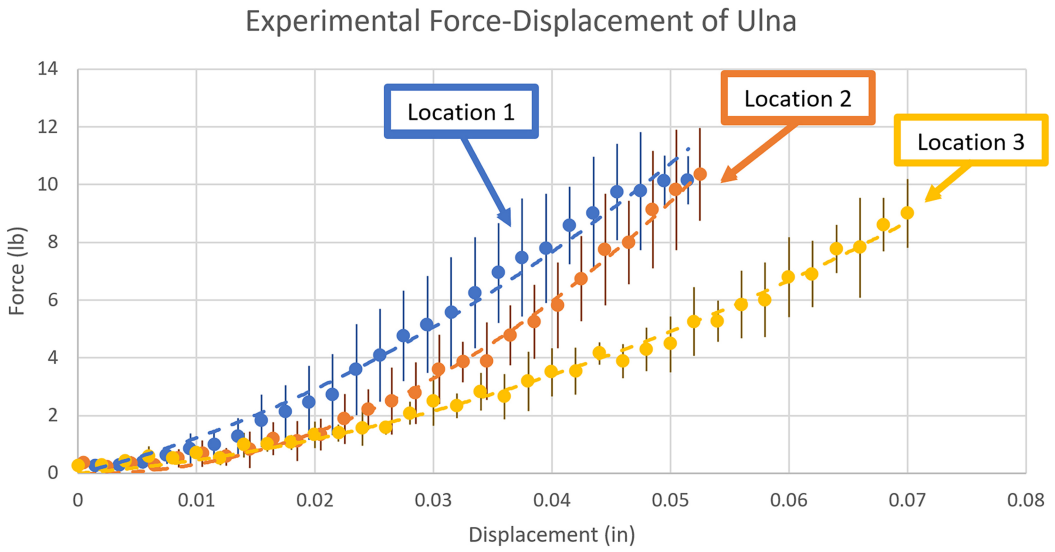

Figure 9. Experimental force-displacement curves for all three locations including the mean and a range of two standard deviations.

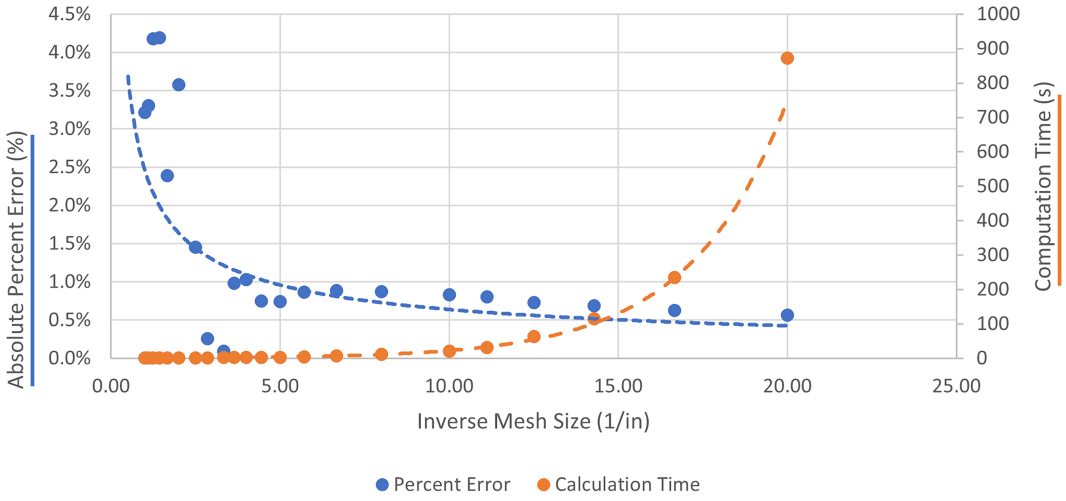

Figure 10. Convergence analysis including the percent error and computation time against the reciprocal of mesh size.

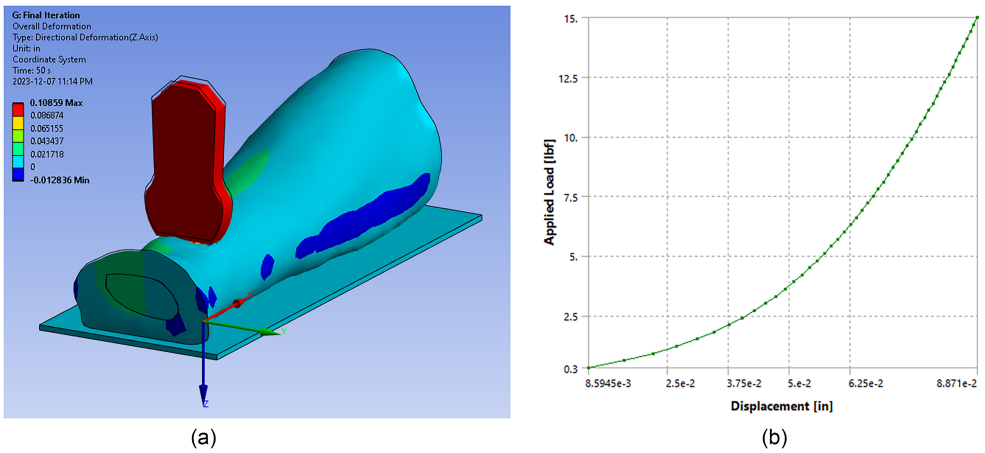

(a) (b)

Figure 11. Deformed finite element model of location 3 with deformation in inches: (a) final iteration and (b) force–displacement results obtained within the finite element program .

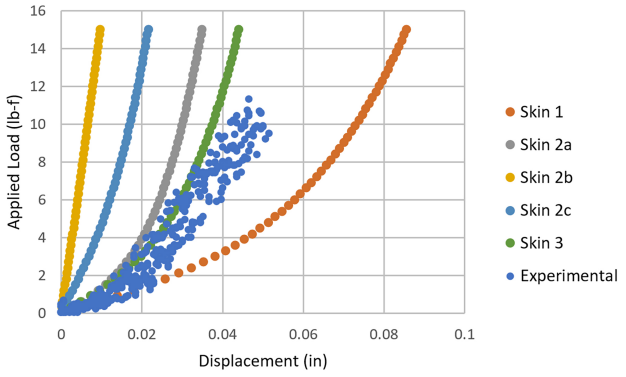

Figure 12. Finite element results using several soft-tissue material properties from the literature vs. experimental data, location 1.

Table 2
Curve-Fit First-Order Ogden Material Parameters

Location	μ (kPa)	α_1	RMSE (lb)	R-Squared
1	9.18	11.24	1.47	0.974
2	2.51	10.08	1.20	0.919
3	2.08	10.75	1.15	0.947

After the curve-fitting process, Bland-Altman plots were generated to evaluate the agreement across the range of displacements [37]. These can be seen in Fig. 14. The blue line represents the mean difference across the entire range of displacements. The dotted orange lines represent the limits of agreement which represent 95% of the differences, or 1.96 standard deviations above and below the mean difference. As shown in the plots, the average is close to zero, indicating that the derived parameters do not consistently over-predict or under-predict results. However, there may be a weak proportional bias which indicates that the derived parameters are more accurate at smaller loads.

3.3 Simplification Results

The original finite element model completed the calculations above with an average CPU time of 920 s. Each model for all three locations contained an average of 23,000 nodes and 115,000 elements.

Four simplified models were developed to investigate how the simplifications may affect both accuracy and computation time. These simplifications were generally limited to changes in the geometry of the model. Factors, such as material properties and mesh parameters were kept constant to reduce the number of variables. However, one additional change was made when simplifying the cylindrical model to the multi-slab model (model 2). The contact formulation detection method was switched from the Augmented Lagrange method to the Multi Point Constraint (MPC) method to have better efficiency in bonded contacts. When making the halved model (model 4), the applied load was halved along with the geometry.

Each model successfully predicted compression load applied to the arm. All four showed similar stiffness characteristics as the original model. The stiffness of each iteration for location 1 can be seen in Fig. 15. The stiffness curves for the remaining two locations can be found in Appendix 2. In general, all simplifications exhibited a larger absolute error at higher loads.

As expected, with each simplification, the computation time decreased. A comparison of the model size and the total computation time of each model can be found on Fig. 16. The simulation calculated 50 discrete steps, thus the average computation time per step is 18.4, 14.4, 6.4, and 0.95 s, respectively. Therefore, all models make incremental cost savings compared to the original model.

The models have also shown with more assumptions and simplifications comes decreasing accuracy. Figure 17 shows the average normalised RSME (NRMSE) across simplifications. NRMSE is used instead of RMSE because the expected magnitude of displacement is different across the three locations, as seen in Fig. 9. The NRMSE was calculated as:

$$\text{NRMSE} = \frac{\text{RMSE}}{x_f} = \frac{\sqrt{\frac{1}{n}\sum_{i=1}^{n}\left[x_o(P_i) - x_s(P_i)\right]^2}}{x_f}, \quad (5)$$

where x_f is the displacement corresponding to the final or maximum load in the original model. The variable n is the number of data points or load steps, which is 50. P_i is the ith load step, which is an input defined prior to running the simulation. x_o and x_s are the outputs or displacements predicted in the original model and simplified model, respectively, at load step P_i.

The cylindrical model has a relatively small NRMSE of 1.8% of the maximum displacement while the multiple-slab, top-reduced, and halved models have a higher NRMSE of 6.1%, 9.0%, and 9.6%, respectively. The R-squared values comparing the results of the simplified models to the original were 1.000, 0.998, 0.994, and 0.996, respectively. Note that some noise may be present in the error from re-meshing the models.

3.4 Discussion

The experiments in this study have resulted in three major outcomes: (1) a phenomenological model of the human wrist, (2) the first-order Ogden material parameters for the soft tissue around the wrist, and (3) an investigation into possible methods to improve the computation time for wrist models.

A time-efficient model of the human wrist to simulate the interaction with external stimuli has many applications. It could potentially be used for virtual simulation, such as for medical training, generating haptic force feedback, or robotic control schemes [16]. The model generated in this study is a step towards real-time modelling and has shown that a detailed representation of the bony structure is not necessary to simulate surface skin deformation. In addition, soft tissue, such as many layers of the skin, fat, and muscle can be approximated with a single phenomenological soft tissue. A benefit of the modelling procedure used in this

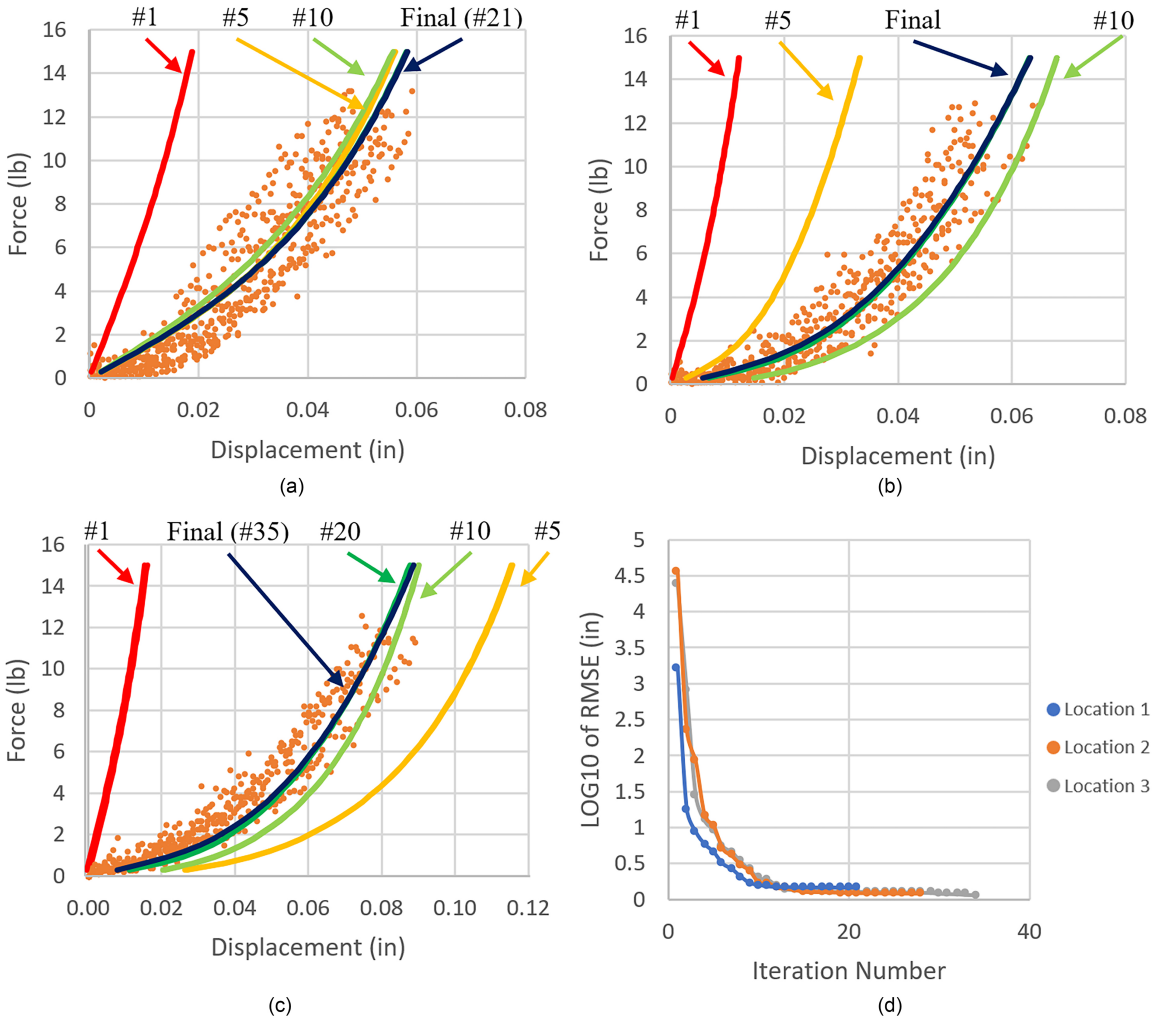

Figure 13. The convergence of the simulated force-displacement curve to the experimental data for (a) location 1; (b) location 2; (c) location 3; and (d) convergence of the average error across the Nelder–Mead optimisation simplex for all three locations.

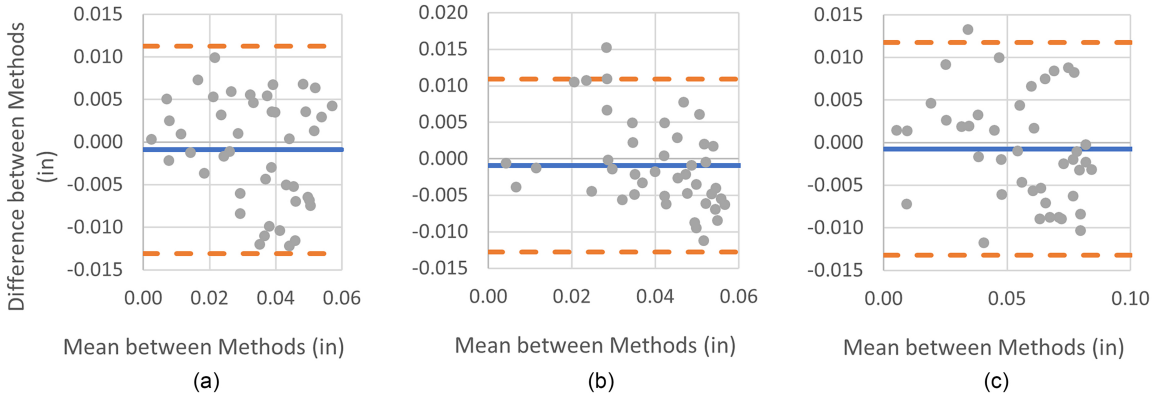

Figure 14. Bland–Altman plots comparing results from experimental trials and simulation with the curve-fitted parameters for (a) location 1; (b) location 2; and (c) location 3.

study is that the skin model has a low technological barrier to entry, requiring only a camera and a computer with appropriate software.

The primary limitation of this model is that it is a subject-specific model which may be only accurate for the original subject. One method to address this problem is to make one or more "average" models to represent a set of people. Additionally, with an average time of 18.4 s per calculation step, this model may not be efficient for real-time applications given the current hardware. However, improving components, such as the CPU and RAM or using more cores may considerably decrease

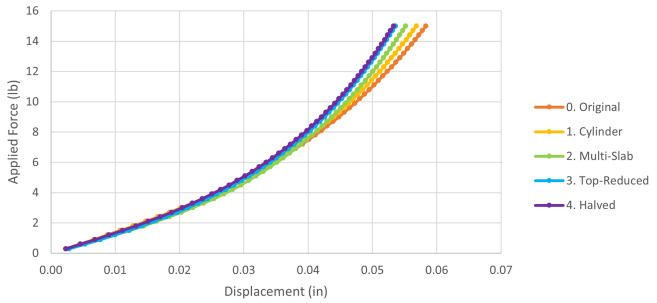

Figure 15. Simplification results: Force–displacement curves across iterations, location 1.

the time. One simple numerical experiment showed that decreasing the number of cores from four to one increased the CPU time by a factor of 3.2.

Using model-correction FEA, the hyperelastic material parameters for soft tissue at the wrist were determined. In general, these first-order Ogden material parameters are in the range of other soft tissues reported in the literature. Additionally, the values found between each location are relatively similar. Location 1 was found to have a larger initial shear modulus, μ, of 9.18 kPa compared to locations 2 and 3 with 2.51 and 2.08 kPa, respectively. This difference is likely due to a change in tissue or potential pre-strain across locations. This type of variation across locations was not unexpected and has been reported in other studies [28]. Future studies could conduct experimental tests on a variety of participants to quantify the typical, non-pathological range for the general population and to investigate differences. Additional variables, such as pre-strain or compressibility, with more precise equipment, could be investigated in future work. Finally, this work can be continued by investigating anatomy, besides the wrist, which has not been reported in the literature.

Additionally, this study investigated simplifications that could be made to improve the computation time of anatomical models. For example, simplifying the arm into an extruded cross-section was shown to be an effective change, reducing the number of elements by 43% with a small average variation of 1.8% NRMSE compared to the original model. This model could be further refined by selecting a better cross-section, such as the "average" cross-section underneath the probe face.

The multi-slab model had an average NRMSE of 6.1% and reduced the CPU time by 65%. Therefore, replacing the cylindrical geometry with laminated slabs improves calculation efficiency while having a minimal increase in error. Some of the error is inherited from the cylindrical model since it was used to estimate the appropriate thickness of each slab. Additionally, the rounded bodies are flattened which may have altered the stiffness behaviour arising from geometry. Besides the time savings, another potential benefit of this model is its flexibility. This model is primarily defined by three variables, the thickness of each slab, and thus could be adjusted to model a variety of people. The model could similarly be used for different orientations of the arm, such as rotation of the wrist.

Both the top-reduced and halved models were developed explicitly for time-efficiency—reducing the computation time. They had a reduced computation time of 83% and 95% compared with the original model's computation time. The halved model calculated each step every 0.95 s which means it can model experimental trials in real-time. This time is reasonable, especially with an asynchronous framework as proposed in [15]. The final model had a RMSE of 9.6% and R-squared value of 0.996. Additionally, the shape of the stiffness curve has been maintained from the original model to the final model, as seen in Fig. 15. A future area of research is to investigate which factors are important for effective haptic feedback in a time-delayed system, such as accuracy of material stiffness, non-linear effects, or prediction reliability. This research would investigate what is required for the model, whether an accurate representation of the biological tissue or only a reasonable, positive force–displacement relationship. This research can inform future model design.

The main constraint of the computer system seemed to be the CPU. Thus, time could be further improved with a faster CPU and using more cores, keeping in mind that increasing the number of cores has decreasing returns. Currently, the software predicting the contact load is independent of the physical system. Work must be done to integrate it into the existing telesonography device. The geometry of the model could also be further improved. For example, the length of the bone and bottom skin could also be reduced, depending on the allowable error. This investigation in model efficiency does not only affect wrist models, but it can also be applied to models of other anatomy, such as fingers, the arms, or legs. The investigation of a rigid manipulator to soft tissue can be reversed to investigate soft robots interacting with their environment.

Another direction of future research includes investigating the effectiveness of different formulations and material models. FEA-A updates the deformation and stiffness matrix every time step for nonlinear geometry. The Ogden function defines how the stress and stiffness matrices are updated based on stretch as derived for this research in (3) [38]. A computer program called SPACAR has been shown to accurately model the interaction between soft and rigid bodies—including forces like a multi-region contact model and friction. In [39], a method for building a kinetic model for steerable catheters, which captures geometric nonlinearity, was presented. The program SPACAR was originally presented in [41]. The program is based on the finite element method for multi-DOF mechanisms. The program, which is written in FORTRAN, can analyse dynamics of spatial mechanisms and manipulators with flexible links; it treats the general motion by coupling large displacement/rotation with small elastic deformation. This program, which has the capability to update stiffness and damping matrices with each time step, is a good alternative for soft and rigid bodies robot motion. However, the program is typically used for small model mechanisms, as the readily available version is limited to 120 DOFs, or 20

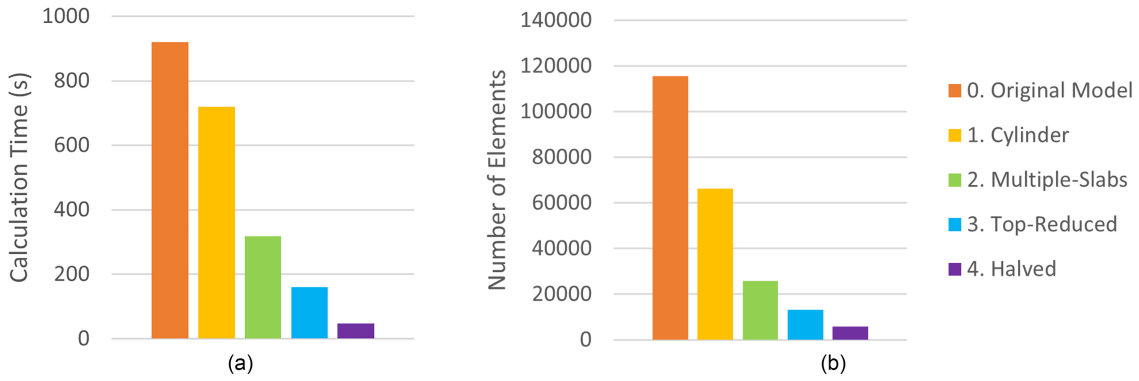

Figure 16. Average simplification results across all three locations: (a) total computation time and (b) model elements.

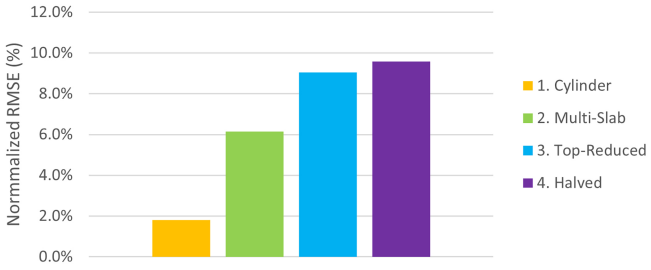

Figure 17. Average measurement error (NRMSE) for all three locations across simplifications.

beam elements with 6 DOFs. Our model would have to be further simplified with a current minimum of 6000 elements in the smallest model. Furthermore, SPACAR program is designed mostly for geometric nonlinearity (large rotations and small elastic deformations), while the case presented in our paper, is mostly deal with material nonlinearity. Alternative solid mechanics model that could be researched is Neo–Hookean solid; this model is a hyper-elastic material model, like Hooke's law, that can be used for predicting the nonlinear stress–strain behaviour of materials undergoing large deformations.

4. Conclusion

This research is part of the MSK-TIM project at the University of Saskatchewan which has developed technology for remote ultrasound diagnosis. A material mode of the wrist can be used to generate force-feedback, which has several applications in human–robot interactions. These include generating haptic feedback, informing control schemes, and software safety systems. Therefore, the goal of this research was to develop a computationally efficient model of the wrist to simulate contact with the external environment. This study consisted of three components: experimentally measuring the stiffness curve of an arm-probe interaction, developing a finite element model to simulate the interaction, and simplifying the model to decrease computation time.

There are three main outcomes of this research. First, it has been shown that a complex model including the anatomical structure of the wrist is not necessary to predict contact behaviour. In this study, several distinct tissues including layers of skin, muscle, and nerves were simplified to a single phenomenological material "soft tissue". The resultant finite element model successfully predicted the non-linear stiffness of the wrist. The second outcome of this research was the determination of the first-order Ogden material parameters of the wrist tissue. While tissue within the upper arm and fingers have been reported, the behaviour of the wrist has been missing from the literature. Finally, this research investigated different methods to simplify anatomical models to decrease computation time. It was shown that the geometry under the area of contact provides most of the structure or stiffness. Simplifications that reduce the non-adjacent geometry were shown to have good efficiency with minimal changes to accuracy. Under similar loading conditions, these techniques can be used to simplify other composite structures, such as the leg or fingers.

Future work in modelling anatomy can investigate how different configurations of the wrist may affect modelling. Alternatively, other anatomy can be modelled. One specific area of interest is using DIC from an ultrasound feed with a model to generate force-feedback. With this technology, the applied force can be accurately estimated for tele-ultrasound, even on commercially available devices that do not have a load cell. Finally, the stiffness characteristics from a large sample should be considered to obtain a statistical analysis of the material parameters and develop techniques to model a range of people.

A. Appendices

A.1 Nelder–Mead Optimisation Procedure

A curve-fitting procedure was used to determine which material parameters can be used with the finite element model to best fit the experimental data. The Nelder–Mead optimisation method was chosen because it is a numerical method and thus it can handle discrete data-points instead of a function [40]. This algorithm can be used for multi-variable functions of two or more parameters. The goal is to match the simulated results to the experimental results; therefore, the objective is to minimise the error between the simulated material and the experimental data. RMSE is used to rank different pairs of material properties—the lower, the better.

Table A1
Initial Points for Material Optimisation Using the Nelder–Mead Algorithm

ID	μ (kPa)	α_1	RMSE (lb-f), location 1
Skin 1 [27]	5.07	9.14	3.54
Skin 2b [28]	39.8	35.5	4985.73
Skin 5 [31]	0.13	26.0	8.34

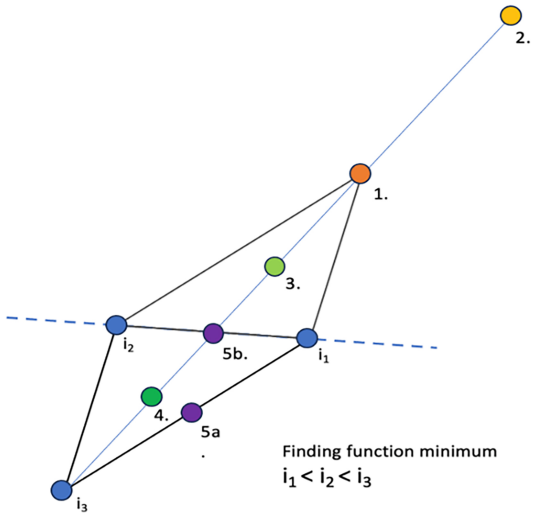

Figure A1. Graphical representation of the Nelder–Mead optimisation method where i_1, i_2, and i_3 are the initial points of the simplex. Points 1, 2, 3, 4 correspond to the proposed points after reflection, extension, contraction of the reflected point, and contraction of the initial point respectively. Points 5a and 5b are the proposed points after shrinking.

The Nelder–Mead algorithm creates a simplex of n + 1 points, where n is the number of variables being optimised. For the material optimisation with two parameters, a simplex of three initial points is needed. Based on the material parameters from the literature found in Table 1, the initial points were chosen as given in Table A1.

The next step is to follow the Nelder–Mead algorithm to find better points. Following this procedure, in most iterations, one of the points of the simplex will be replaced with a better point. However, these improvements will get smaller as the simplex approaches the minima and gets smaller in size.

The generalised algorithm has four operations to generate the next point in the simplex: reflection, extension, contraction, and shrinking. A visual representation of the next generated point according to the algorithm is shown in Fig. A1.

Without an end condition, this iteration may continue indefinitely. Therefore, it is important to choose an end-condition which will find a balance between precision and efficiency. For this research, two end-conditions were given which must both be met:

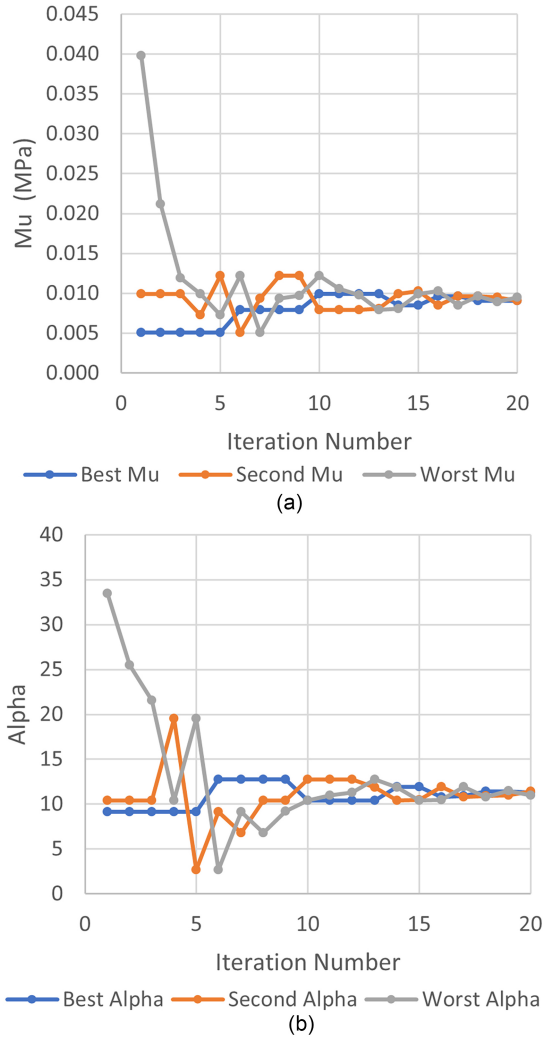

Figure A2. Points on the Nelder–Mead simplex converging over iterations for location 1: (a) Mu and (b) Alpha.

1. The standard deviation of the RMSE across the three points must be less than 1% of the mean for five consecutive iterations.
2. The standard deviation of the final parameters across the three points must be less than 10% of the mean.

This combination on end conditions ensure that the optimisation has truly converged and that the final parameters are known with a reasonable level of certainty. The result of the optimisation procedure can be seen in Fig. A2 below, plotting the convergence for each material parameters across iterations.

A.2 Supplemental Figures

Figure 15 showed the effects of different simplification steps for location 1. However, for a more complete view, Figs. A3 and A4 have been added to this appendix. These two figures show the effects of simplification for location 2 and location 3, respectively.

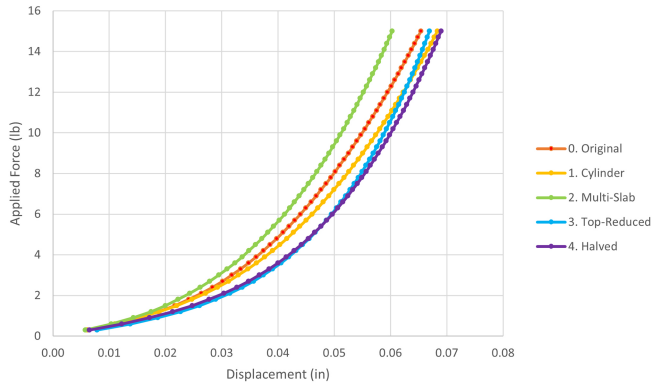

Figure A3. Force–displacement curves across iterations, location 2.

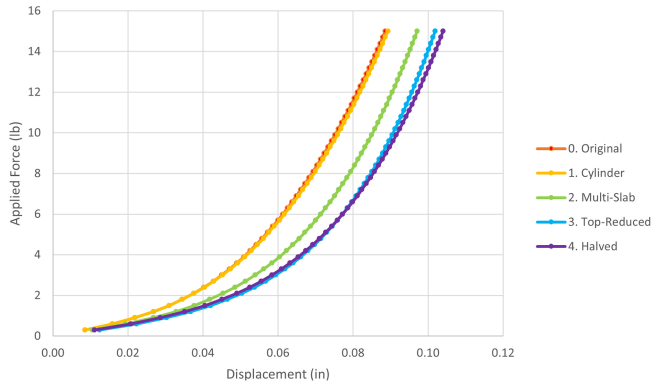

Figure A4. Force–displacement curves across iterations, location 3.

Acknowledgement

Our deepest gratitude to the members of the Robotics Lab at the University of Saskatchewan for their prior work on the MSK-TIM project, especially to Qianwei Zhang for his contribution to the design and implementation of the MSK robot as well as its control software.

Author Contributions

Z.O. was the main contributor for the content of this research, performed experiements, analyzed the data, and wrote the manuscript. R.F. was the principal investigator, supervised the research, reviewed the analyses, edited the paper, and co-funded this research. H.O. contributed to editing the paper and co-funded this research. All authors have read and agreed to the published version of the manuscript.

Funding

We would like to acknowledge the University of Saskatchewan, College of Medicine, and Royal University Hospital Foundation for financially supporting the development of the MSK robot. Funding from the Natural Sciences and Engineering Research Council of Canada is also acknowledged.

Competing Interests

The authors have no relevant financial or non-financial interests to disclose.

References

[1] H. Oflaz and I. Gunal, Maximum loading of carpal bones during movements: A finite element study, *European Journal of Orthopaedic Surgery & Traumatology.*, *29*(1), 2019, 47–50, DOI: http://dx.doi.org/10.1007/s00590-018-2287-7.

[2] E. Rothenfluh, S. Jain, R. Guggenberger, W.R. Taylor, and S.H. Hosseini Nasab, The influence of partial union on the mechanical strength of scaphoid fractures: A finite element study, *Journal Journal of Hand Surgery European Volume*, *48*(5), 2023, 435–444, DOI: http://dx.doi.org/10.1177/17531934231157565.

[3] D. E. Mouzakis, G. Rachiotis, S. Zaoutsos, A. Eleftheriou, and K. N. Malizos, Finite element simulation of the mechanical impact of computer work on the carpal tunnel syndrome, *Journal Biomechanics*, *47*(12), 2014, 2989–2994, DOI: http://dx.doi.org/10.1016/j.jbiomech.2014.07.004.

[4] S. Peshin, Y. Karakulova, and A. G. Kuchumov, Finite element modeling of the fingers and wrist flexion/extension effect on median nerve compression, *Applied Sciences*, *13*(2), 2023, 2, DOI: http://dx.doi.org/10.3390/app13021219.

[5] B. Faudot, J. Ballerini, M. Ross, P. Bellemère, B.G. de Monsabert, L. Vigouroux, and J.L. Milan, Mechanical performance comparison of two surgical constructs for wrist four-corner arthrodesis via dorsal and radial approaches, *Clinical Biomechanics.*, *82*, 2021, 105274, , DOI: http://dx.doi.org/10.1016/j.clinbiomech.2021.105274.

[6] M. Kim, G. Pons-Moll, S. Pujades, S. Bang, J. Kim, M.J. Black, and S.H. Lee, Data-driven physics for human soft tissue animation, *ACM Transactions on Graphics*, *36* (4), 2017, 1–54, DOI: http://dx.doi.org/10.1145/3072959.3073685.

[7] A. Mena, R. Wollstein, J. Baus, and J. Yang, Finite element modeling of the human wrist: A review, *Journal of Wrist Surgery*, *12*(106), 2023, 478–487, DOI: http://dx.doi.org/10.1055/s-0043-1768930.

[8] L. Peng, Y. Wu, K. Lakshminarayanan, A. Zhang, Y. Gan, Y. Li, and Y. Yao, The relationship between shear wave velocity in transverse carpal ligament and carpal tunnel pressure: A finite element analysis, *Medical Engineering & Physics*, *116*2023, 103995, DOI: http://dx.doi.org/10.1016/j.medengphy.2023.103995.

[9] M.K. Gislason, E. Foster, M. Bransby-Zachary, and D.H. Nash, Biomechanical analysis of the universal 2 implant in total wrist arthroplasty: A finite element study, *Computer Methods in Biomechanics and Biomedical Engineering*, *20* (10), 2017, 1113–1121, DOI: http://dx.doi.org/10.1080/10255842.2017.1336548.

[10] G. Limbert, Mathematical and computational modelling of skin biophysics: A review, *Proceedings of the Royal Society A: Mathematical, Physical and Engineering Sciences*, *473*(2203), 2017, 20170257, DOI: http://dx.doi.org/10.1098/rspa.2017.0257.

[11] Z. Ochitwa, R. Fotouhi, S. J. Adams, A. P. Noguera Cundar, and H. Obaid, MSK-TIM: A telerobotic ultrasound system for assessing the musculoskeletal system, *Sensors*, *24*(7), 2024, 7, DOI: http://dx.doi.org/10.3390/s24072368.

[12] L. Santos, R. Cortesão, and J. Quintas, Twin kinematics approach for robotic-assisted tele-echography, in *Proceeding IEEE/RSJ International Conference on Intelligent Robots and Systems (IROS)*, Macau, 2019, 1339–1346, DOI: http://dx.doi.org/10.1109/IROS40897.2019.8968481.

[13] A. Saracino, A Deguet, F Staderini, MN Boushaki, F Cianchi, A Menciassi, and E Sinibaldi, Haptic feedback in the da Vinci Research Kit (dVRK): A user study based on grasping, palpation, and incision tasks, *The International Journal of Medical Robotics and Computer*, *15*(4),2019, e1999, DOI: http://dx.doi.org/10.1002/rcs.1999.

[14] L. Wijayarathne, Z. Zhou, Y. Zhao, and F.L. Hammond, Real-time deformable-contact-aware model predictive control

for force-modulated manipulation, *IEEE Transactions on Robotics*, *39*(5), 2023, 3549–3566, DOI: http://dx.doi.org/10.1109/TRO.2023.3286070.

[15] A. Munawar and G. S. Fischer, An asynchronous multi-body simulation framework for real-time dynamics, haptics and learning with application to surgical robots, in *Proceeding IEEE/RSJ International Conference on Intelligent Robots and Systems (IROS)*, Macau, 2019, 6268–6275, DOI: http://dx.doi.org/10.1109/IROS40897.2019.8968594.

[16] P. Barattini, F. Vicentini, G. S. Virk, and T. Haidegger, Eds., *Human-Robot Interaction: Safety, Standardization, And Benchmarking*. (Boca Raton, FL: CRC Press, Taylor & Francis Group, 2019).

[17] A. Murai, Q. Youn Hong, K. Yamane, and J. K. Hodgins, Dynamic skin deformation simulation using musculoskeletal model and soft tissue dynamics, *Computational Visual Media*, *3*(1), 2017, 49–60, DOI: http://dx.doi.org/10.1007/s41095-016-0065-1.

[18] M. Obaid, Q. Zhang, S.J. Adams, R. Fotouhi, and H. Obaid, Development and assessment of a telesonography system for musculoskeletal imaging, *European Radiology Experimental*, *5*(29), 2021, 1–9, DOI: http://dx.doi.org/10.1186/s41747-021-00227-z.

[19] C. Ulrich and L.N.S. Andreasen Struijk, Probe contact forces during obstetric ultrasound scans-a design parameter for robot-assisted ultrasound, *International Journal of Industrial Ergonomics*, *86*, 2021, 103224, DOI: http://dx.doi.org/10.1016/j.ergon.2021.103224.

[20] M. Dhyani, S.C. Roll, M.W. Gilbertson, M. Orlowski, A. Anvari, Q. Li, B. Anthony, and A.E. Samir, A pilot study to precisely quantify forces applied by sonographers while scanning: A step toward reducing ergonomic injury, *Work*, *58*(2), 2017, 241–247, DOI: http://dx.doi.org/10.3233/WOR-172611.

[21] A. Freitas, MRI Wrist Anatomy, Musculoskeletal MRI. Accessed: Jul. 21, 2023. [Online]. Available: https://www.freitasrad.net/pages/atlas/Wrist/Wrist.php

[22] R. W. Ogden, *Non-linear Elastic Deformations*. (Mineola, NY: Dover Publications, 1997).

[23] S. D. Łagan and A. Liber-Kneć, Experimental testing and constitutive modeling of the mechanical properties of the swine skin tissue, *Acta of Bioengineering and Biomechanics*, *19*(2), 2017, 93–102, DOI: http://dx.doi.org/10.5277/ABB-00755-2016-02.

[24] D. C. Lin, D. I. Shreiber, E. K. Dimitriadis, and F. Horkay, Spherical indentation of soft matter beyond the Hertzian regime: Numerical and experimental validation of hyperelastic models, *Biomechanics and Modeling in Mechanobiology*, *8*(5), 2009, 345–358, DOI: http://dx.doi.org/10.1007/s10237-008-0139-9.

[25] P. Martins, R M. Natal Jorge, and A.J.M. Ferreira, A comparative study of several material models for prediction of hyperelastic properties: Application to silicone-rubber and soft tissues, *Strain*, *42*(3), 2006, 135–147, DOI: http://dx.doi.org/10.1111/j.1475-1305.2006.00257.x.

[26] G. A. Holzapfel and R. W. Ogden, *Mechanics of Biological Tissue*. (Berlin,: Springer, 2006). Accessed: Mar. 21, 2023. [Online]. Available: http://ebookcentral.proquest.com/lib/usask/detail.action?docID=304247

[27] F. Mo, Z. Zheng, H. Zhang, G. Li, Z. Yang, and D. Sun, In vitro compressive properties of skeletal muscles and inverse finite element analysis: Comparison of human versus animals, *J. Biomech.*, *109*, 2020, 109916, DOI: http://dx.doi.org/10.1016/j.jbiomech.2020.109916.

[28] C. Flynn, A. Taberner, and P. Nielsen, Mechanical characterisation of in vivo human skin using a 3D force-sensitive micro-robot and finite element analysis, *Biomechanics and Modeling in Mechanobiology*, *10*(1), 27–38, 2011, DOI: http://dx.doi.org/10.1007/s10237-010-0216-8.

[29] C. Noël, A three-dimensional visco-hyperelastic FE model for simulating the mechanical dynamic response of preloaded phalanges, *Medical Engineering & Physics*, *61*, 2018, 41–50, DOI: http://dx.doi.org/10.1016/j.medengphy.2018.08.007.

[30] A. Aldieri, M. Terzini, C. Bignardi, E. M. Zanetti, and A. L. Audenino, Implementation and validation of constitutive relations for human dermis mechanical response, *Medical & Biological Engineering & Computing.*, *56*(11), 2018, 2083–2093, DOI: http://dx.doi.org/10.1007/s11517-018-1843-y.

[31] S.L. Evans and C.A. Holt, Measuring the mechanical properties of human skin in vivo using digital image correlation and finite element modelling, *The Journal of Strain Analysis for Engineering Design44*(5), 2009, 337–345, DOI: http://dx.doi.org/10.1243/03093247JSA488.

[32] N.K. Sharma, S. Sharma, A. Rathi, A. Kumar, K.V. Saini, M.D. Sarker, S. Naghieh, L. Ning, and X. Chen, Micromechanisms of cortical bone failure under different loading conditions, *Journal of Biomechanical Engineering142*, 2020, 94501, DOI: http://dx.doi.org/10.1115/1.4046688.

[33] Q. Grimal, S. Haupert, D. Mitton, L. Vastel, and P. Laugier, Assessment of cortical bone elasticity and strength: Mechanical testing and ultrasound provide complementary data, *Medical Engineering & Physics31*(9), 2009, 1140–1147, DOI: http://dx.doi.org/10.1016/j.medengphy.2009.07.011.

[34] N. Haji, R. Fernandez, L. Haji, B. Jawad, H. Vejdani, and V. Fernandez, "Optical full-field strain visualization on bone," presented at the ASME 2022 International Mechanical Engineering Congress and Exposition, American Society of Mechanical Engineers Digital Collection, 2023, DOI: http://dx.doi.org/10.1115/IMECE2022-96154.

[35] M.J. Lohr, G.P. Sugerman, S. Kakaletsis, E. Lejeune, and M.K. Rausch, "An introduction to the Ogden model in biomechanics: Benefits, implementation tools and limitations," *Philosophical Transactions of the Royal Society A.*, *380*(2234), 2022, 20210365, DOI: http://dx.doi.org/10.1098/rsta.2021.0365.

[36] N. Rajaei, T. Fujikawa, and Y. Yamada, "Experimental investigation of human soft tissue behavior for constructing human-robot contact force-displacement measuring system," in *Proceeding of the IEEE International Conference on Intelligence and Safety for Robotics*, Nagoya , 2021, 15–19.

[37] J. M. Bland and D. G. Altman, Measuring agreement in method comparison studies, *Statistical Methods in Medical Research.*, *8*(2), 1999, 135–160, DOI: http://dx.doi.org/10.1177/096228029900800204

[38] *ANSYS 2022 R1 Mechanical APDL Theory Reference*, ANSYS, Inc., Canonsburg PA, 2022.

[39] X. Hu, L. Cao, Y. Luo, A. Chen, E. Zhang, and W. J. Zhang, A novel methodology for comprehensive modeling of the kinetic behavior of steerable catheters, *IEEEASME Transactions on Mechatronics*, *24*(4), 2019, 1785–1797, DOI: http://dx.doi.org/10.1109/TMECH.2019.2928786.

[40] C. Audet and W. Hare, *Derivative-Free and Blackbox Optimization*, in Springer Series in Operations Research and Financial Engineering. (Cham: Springer, 2017), DOI: http://dx.doi.org/10.1007/978-3-319-68913-5.

[41] B. Jonker, *A finite element dynamic analysis of flexible spatial mechanisms and manipulators*, Ph.D. Thesis, Technische Universiteit Delft, Netherlands, 1988. www.researchgate.net/publication/27349230.

[42] X. Zhu, K. Zhang, and X. Hua, Consistency analysis and suggestions of collision measurement in human-robot collaboration safety evaluation, *International Journal of Robotics and Automation*, *39*(10), 2024, 1–13, DOI: http://dx.doi.org/10.2316/J.2024.206-1058.

[43] X. Yan and P. Liu, Kinematic analysis and design of a haptic device for neurosurgery simulation, *International Journal of Robotics and Automation*, *38*(1), 2023, 60–66, DOI: http://dx.doi.org/10.2316/J.2023.206-0770.

Biographies

Reza Fotouhi has been a Professor of Mechanical Engineering with the University of Saskatchewan, Saskatoon, Canada, since 2002. He has established and is the Director of the Robotics Lab, University of Saskatchewan. He is well known in robotics research communities in Canada and USA. His research interests include robotics (dynamics & control), structural dynamics and vibrations, computational mechanics, and biomechanics. his current research is focussed on control of industrial manipulators and mobile robots. He is an Associate Editor for *ASME Journal of Mechanism and Robotics* and *International Journal of Robotics and Automation*, ACTA press.

Haron Obaid is a Professor of Musculoskeletal Radiology with the College of Medicine, University of Saskatchewan, Canada. He completed the Radiology residency with the University of Leicester, U.K. followed by musculoskeletal fellowship training at the University of Toronto. He is board certified in Diagnostic Radiology in the UK and Canada. He published book chapters and a number of articles in international peer reviewed journals. His research interests are in quantitative MRI imaging and telerobotic musculoskeletal ultrasound. He is a member of the International Skeletal Society since and Skeletal Radiology editorial board. He is an Associate Editor for the journal of *British Journal of Radiology* Open.

Zachary Ochitwa received the M.Sc. degree in mechatronics from the Department of Mechanical Engineering, University of Saskatchewan, Canada. His specialisation is in control, robotics, and finite-element analysis and has worked on robots in medicine, agriculture, and mining. He is currently working in Applied R&D Engineering in Saskatoon, SK, Canada.